nanomaterials

MDPI

Article

Heavy-Ion Irradiation of Porous Silicon with Functional Nanocoatings

Hanna Bandarenka [1,2,*], Diana Laputsko [2], Aliaksandr Burko [2], Veronika Koshkarova [2], Valeryia Murashka [2], Zhuldys Nurlan [3], Abdirash Akilbekov [3] and Alma Dauletbekova [3,*]

[1] School of Physical, Chemical and Environmental Sciences, Department of Physics and Astronomy, Cardiff University, Cardiff CF24 3AA, UK
[2] Applied Plasmonics Laboratory, Belarusian State University of Informatics and Radioelectronics, 220013 Minsk, Belarus; d.laputko@bsuir.by (D.L.); a.burko@bsuir.by (A.B.); v.koshkarova@bsuir.by (V.K.); v.murashko@bsuir.by (V.M.)
[3] Department of Technical Physics, L.N. Gumilyov Eurasian National University, Astana 010000, Kazakhstan; zhuldyz.nurlan.99@mail.ru (Z.N.); akilbekov_at@enu.kz (A.A.)
* Correspondence: bandarenkah1@cardiff.ac.uk (H.B.); alma_dauletbek@mail.ru (A.D.)

Abstract

This study investigates the structural, morphological, and elemental modifications induced by swift heavy-ion irradiation in functionalized multilayer nanomaterials. Macroporous silicon (macroPSi) substrates coated with 100-nm titanium dioxide (TiO_2) thin films via atomic layer deposition were decorated with silver nanoparticles (AgNPs) synthesized by magnetron sputtering and subsequent vacuum dewetting. The substrates were bombarded with $^{40}Ar^{8+}$ (70 MeV) and $^{132}Xe^{22+}$ (220 MeV) ions at 10^{10} cm^{-2} and 10^{11} cm^{-2} fluences, respectively. Combined scanning electron microscopy (SEM) and energy-dispersive X-ray (EDX) spectroscopy revealed surface pitting and an increase in average pore diameter of $14.0 \pm 0.3\%$ (Ar^{8+}) and $40 \pm 0.8\%$ (Xe^{22+}) in Ag-free macroPSi/TiO_2. Multilayer SRIM/TRIM calculations give electronic stopping powers in the TiO_2 film of 6.768 keV/nm for Ar and 23.340 keV/nm for Xe. The Xe value exceeds the literature threshold for anatase, whereas the Ar value lies near that threshold. This comparison concerns the oxide film and does not establish latent-track formation in the silicon framework. In Ag-decorated samples, surface smoothing accompanies pore-entry expansion of $15 \pm 0.3\%$ (Ar^{8+}) and $28 \pm 0.6\%$ (Xe^{22+}). These observations indicate that surface metallization modifies the morphological response under the irradiation conditions investigated. The role of nanoparticle interfaces requires further investigation because the transport model does not explicitly resolve AgNPs.

Keywords: macroporous silicon; titanium dioxide (TiO_2); silver nanoparticles; swift heavy ions; radiation effects

Check for updates

Academic Editors: Jian He and Wenbo Gong

Received: 5 October 2026
Revised: 9 November 2026
Accepted: 16 November 2026
Published: 18 November 2026

Copyright: © 2026 by the authors. Licensee MDPI, Basel, Switzerland. This article is an open access article distributed under the terms and conditions of the Creative Commons Attribution (CC BY) license.

1. Introduction

In recent years, porous semiconductors decorated with functional nanocoatings have emerged as a highly promising class of multilayered nanomaterials for advanced technologies, spanning environmental remediation [1,2], green energy conversion [3,4], and ultra-sensitive molecular analysis [5,6]. Among various host frameworks, porous silicon (PSi) functionalized with metal oxide thin films and metallic nanostructures has attracted significant attention due to its unique structural and optical properties [7,8]. In particular, the modification of PSi with photocatalytic titanium dioxide (TiO_2) thin films and plasmonic silver nanoparticles (AgNPs) offers a hybrid platform possessing unique optical properties [9,10]. For example,

these multicomponent heterostructures can successfully exploit the complementary mechanisms of photocatalytic degradation pathways and electromagnetic field localization via surface-enhanced Raman scattering (SERS) [11]. Consequently, such dual-functionalized systems can exhibit great potential for the visual identification of trace molecular analytes, real-time environmental monitoring, self-cleaning filtration, and targeted antibacterial applications. Despite their remarkable potential, the efficiency of PSi/TiO_2/Ag structures is severely constrained by intrinsic material limitations. Standard chemical [12–14] and physical vapour [15,16] deposition methods typically yield smooth, continuous interfaces and highly crystalline lattices. While structurally uniform, these pristine interfaces lack a sufficient density of active surface defects, such as oxygen vacancies, which are vital for establishing active charge-trapping sites that accelerate photocatalytic pathways by suppressing electron–hole recombination [17]. Furthermore, conventional deposition techniques frequently lead to structural constraints, including restricted molecular diffusion within unoptimized pore channels and the distribution of plasmonic 'hot-spots' necessary for high-sensitivity SERS analysis [18]. Resolving these bottlenecks requires a precise material processing methodology capable of simultaneously manipulating pore geometries, engineering localized surface defects, and controlling multilayered elemental distributions without destroying or mechanically degrading the underlying PSi matrix. Finding such a non-destructive post-synthetic tuning technique remains a significant challenge in nanomaterials science.

Swift heavy ion irradiation can be successfully used as a controlled modification procedure to intentionally engineer defects and morphology within different materials [19–22]. Unlike conventional thermal or chemical treatments, high-energy heavy ion bombardment applies energy primarily through electronic stopping power (S_e), inducing localized electronic excitations and subsequent rapid energy transfer to the atomic lattice [23–25].

The main objective of this work was to comprehensively evaluate how parameters of high-energy heavy Ar^{8+} and Xe^{22+} ions, including kinetic energy levels and ion fluences, alter the surface morphology, pore metrics, and elemental atomic composition of TiO_2-coated macroporous silicon (macroPSi) before and after decoration with AgNPs. To interpret the experimental morphology of the samples, Stopping and Range of Ions in Matter/Transport of Ions in Matter (SRIM/TRIM) calculations were performed for both ion species in the layered TiO_2/Si structure. Electronic and nuclear energy depositions were evaluated separately in each constituent, with threshold comparisons restricted to the same material. A contribution of metallic nanoparticles was assessed by comparing structures with and without Ag. Through a detailed analysis using scanning electron microscopy (SEM) and energy-dispersive X-ray (EDX) spectroscopy, we mapped the radiation-induced defect structures to the physical optimization profiles required for advanced applications. By demonstrating a convergence between numerical calculations and actual morphological evolution, this research shows that swift heavy ion irradiation can be further exploited as a promising processing route to establish predictive control of PSi samples with functional nanocoatings.

2. Materials and Methods

2.1. Fabrication of Macroporous Silicon

MacroPSi layers were formed using single-crystal p-type (boron-doped) silicon wafers with a crystal orientation of (100) and a resistivity of 12 $\Omega \cdot$ cm (Kamerton Branch of Integral JSC, Pinsk, Republic of Belarus). Prior to processing, the Si wafers underwent a 15-min liquid-phase chemical cleaning in a peroxide–ammonia solution (PAS). The PAS consisted of NH_4OH (25%), H_2O_2 (30%), and H_2O mixed in a 1:1:5 volume ratio maintained at a 75 °C temperature. Following this stage, the wafers were rinsed for 5 min in distilled water and subsequently dried inside a centrifuge under an ambient air atmosphere. The cleaned wafers were manually sectioned using a tungsten carbide scriber to yield square experimental samples

with a 9 cm^2 area. Immediately preceding electrochemical etching, individual silicon samples were treated for 30–40 s in a dilute 4–5% aqueous hydrofluoric acid (HF) bath to remove the native silicon dioxide (SiO_2) layer. The electrochemical synthesis (anodization) of the macroPSi layers was carried out in a two-electrode cell integrated with a Metrohm AUTOLAB PGSTAT 302N potentiostat–galvanostat (Metrohm Autolab B.V., Utrecht, The Netherlands). The electrochemical cell was constructed from polytetrafluoroethylene (PTFE) to guarantee chemical inertness against reactive fluoride species (Figure 1).

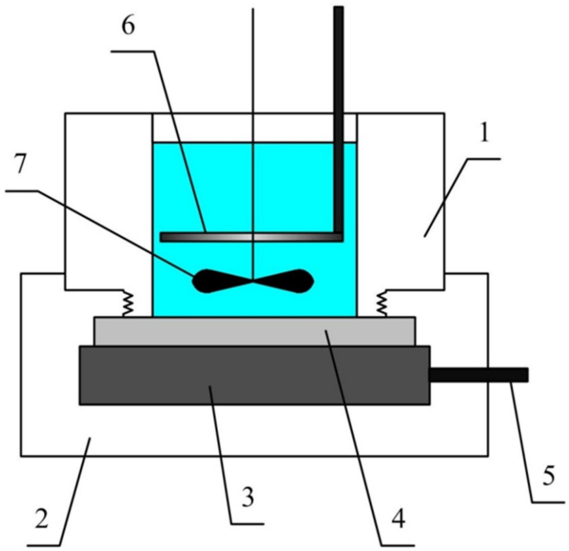


Figure 1. Schematic representation of the electrochemical cell: (1) the upper PTFE cup filled with the electrolyte (blue), (2) the bottom PTFE base, (3) graphite electrode, (4) Si substrate, (5) Cu electrode, (6) Pt electrode, (7) mechanical stirrer.

To ensure a highly uniform current density vector across the entire active area, the substrate was secured against a bottom-mounted, highly polished graphite disc electrode enclosed within the cell base. The cell's liquid sealing interface was achieved by precision polishing the lower rim of the upper PTFE cup parallel to the graphite plane, yielding an active etching window with an open diameter of 2 cm. A coiled platinum wire spiral was employed as the counter-electrode to maintain an even distribution of current density lines within the electrolyte bath. A mechanical stirrer shaft coupled with an impeller driven by an external electric motor was continuously operated inside the fluid volume. This assembly ensured constant replenishment of active chemical reactants at the liquid–solid phase boundary, accelerated the desorption of reaction by-products, and continuously removed evolving hydrogen bubbles to prevent spatial non-uniformities across the macroPSi surface. To enable reliable electrical contact against the graphite base plate, a 3 µm-thick aluminium layer was pre-deposited onto the reverse side of the p-Si substrates via magnetron sputtering. MacroPSi layers featuring arrays of vertical channels were etched using an electrolyte solution consisting of HF (45%) and dimethyl sulfoxide [$(CH_3)_2SO$, DMSO] mixed in a volumetric ratio of 10:48 (Figure 2). Anodization was conducted at a fixed current density of 7 mA/cm^2 for an etching duration scaled between 7 and 10 min. The freshly etched macroPSi was subjected to a post-etch optimization step for the removal of a thin microPSi layer that typically accumulates along the internal macropore walls, which can restrict subsequent deposition of conformal TiO_2 films [7]. This step consisted of sample immersion in a 5 % KOH aqueous solution for 5 min at room temperature.

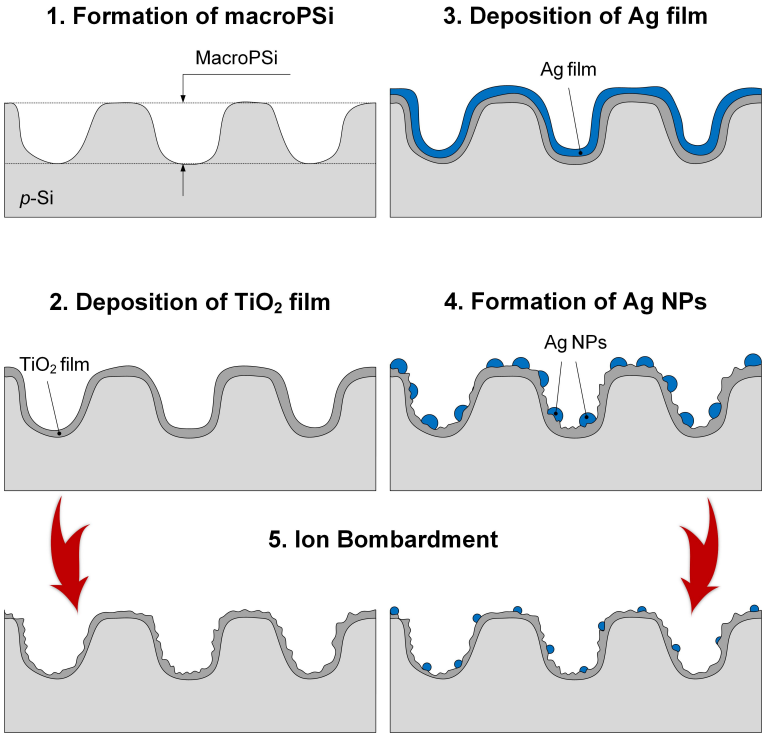


Figure 2. Scheme detailing the stages of the experimental sample fabrication and subsequent ion-beam modification process: (1) electrochemical anodic etching of Si substrates in an HF:DMSO electrolyte to yield macroPSi channels; (2) ALD achieving 100-nm thick TiO_2 film; (3) magnetron sputtering of Ag film; (4) thermal dewetting creating AgNPs; and (5) swift heavy ion bombardment of the samples.

2.2. Deposition of Titanium Dioxide Film

As schematically shown in (Figure 2), TiO_2 thin film with a thickness of 100 nm was grown directly over the macroPSi channels using an atomic layer deposition (ALD) system TFS200 (Beneq, Espoo, Finland). The titanium chemical source consisted of high-purity organometallic tetrakis(dimethylamido) titanium [$Ti(N(CH_3)_2)_4$, TDMAT], which was delivered into the reaction zone using a high-purity argon (Ar) carrier gas stream flowing at a stable rate of 200 cm^3/min. Molecular oxygen (O_2) acted as the co-reactant gas and was introduced via a top-mounted port coupled to an inductively coupled plasma (ICP) source operating at an excitation power of 300 W. The ALD execution loop included the steps of (i) the precursor pulse (TDMAT vapor injection) for 2 s, (ii) the inert gas sweep (Ar purge channel) for 3 s, (iii) the mass-flow and reaction chamber pressure stabilization for 2 s, (iv) the radio-frequency plasma discharge (O_2 ICP activation at 300 W) for 3 s, and (v) the post-reaction purge (Ar carrier gas flush) for 2 s.

2.3. Growth of Silver Nanoparticles

Silver film was deposited over the macroPSi/TiO_2 layers using a MARS-100 magnetron sputtering system (BSUIR, Minsk, Republic of Belarus). The substrates were secured to a bottom-mounted substrate stage using high-vacuum double-sided adhesive tape. A high-purity silver target was installed onto an upper magnetron gun arranged in a top-down sputtering geometry. The target-to-substrate throw distance was held constant at ~20.5 cm. Prior to initiating plasma ignition, the main process chamber was evacuated to a base vacuum level of $\sim 6.5 \cdot 10^{-5}$ Pa. To eliminate spatial non-uniformities in film thickness across the porous network, the substrate stage was continuously rotated about its central perpendicular axis. Sputtering was performed in a high-purity plasma ambient sustained by introducing argon molecules at a controlled mass flow rate of 4.5 cm^3/min, which raised

the operational working pressure to 0.1 Pa. The absolute thickness of the depositing metal layer was dynamically tracked using a calibrated quartz crystal microbalance (QCM) sensor situated immediately to the left of the substrate holder plane. Sputtering power parameters were adjusted to maintain a stable metal growth rate between 1.0 and 1.5 Å/s. To fabricate silver nanoparticles (AgNPs), thin silver film with a thickness of 5–7 nm was deposited (Figure 2). This film was then subjected to a solid-state dewetting process by elevating the substrate stage temperature to 200 °C for 15 min under high-vacuum conditions.

2.4. Swift Heavy Ion Irradiation

Both bare macroPSi/TiO_2 and AgNP-decorated macroPSi/TiO_2 structures were exposed to swift heavy ion bombardment using the IC 100 (JINR, Dubna, Russia) and DC-60 (Astana, Kazakhstan). To examine structural rearrangements under different electronic stopping power regimes, two separate ion configurations were tested, including Ar^{8+} ion beams tuned to a total kinetic energy of 70 MeV and Xe^{22+} ion beams accelerated to an operational kinetic energy of 220 MeV (Figure 2). Irradiation experiments were carried out at room temperature under high-vacuum conditions. The total integral ion doses (fluences) delivered to the sample were 10^{10} cm^{-2} for Ar^{8+} and 10^{11} cm^{-2} for Xe^{22+}. The ion beam current was held below 100 nA throughout the exposures to eliminate unintentional macroscopic beam-heating artifacts.

2.5. Characterization Techniques

The surface and cross-sectional morphologies of the samples before and after ion beam processing were evaluated via SEM. High-resolution SEM micrographs were captured on a Hitachi S-4800 system (Hitachi, Ltd., Tokyo, Japan). Statistical tracking of changes in pore geometry, mouth widening, and average equivalent pore diameters (D) from the SEM data was carried out using ImageJ software (version 1.47i, National Institutes of Health, Bethesda, MD, USA). The structural statistical analysis was systematically executed across multiple independent SEM fields of view, evaluating a total randomized population of $N = 150$ individual macropores per distinct sample state. To mathematically validate the thresholds of radiation-induced structural dilation, a two-tailed independent Student's t-test was conducted [26,27]. Mean values were evaluated against a strict confidence interval, with a threshold of $p < 0.01$ designated to establish statistically highly significant variations between the pristine and ion-irradiated structures.

Localized elemental atomic concentrations and chemical composition transitions across the interfaces were analyzed via EDX spectroscopy. The compositional profiles were recorded using a Link Analytical AN 10000 EDX spectrometer (Oxford Instruments, Abingdon, UK) integrated directly into a Cambridge Instruments Stereoscan-360 SEM (Cambridge Instruments Ltd., Cambridge, UK). The analytical parameters were maintained at a stable electron probe diameter of ~1 µm paired with an acceleration voltage of ~20 keV. This electronic configuration provided a nominal information collection depth constrained between 1.3 and 1.5 µm below the outer surface plane. It should be noted that a high content of carbon was detected in all EDX spectra. This is primarily attributed to electron-beam-induced carbon deposition from residual hydrocarbons in the chamber under standard high-vacuum conditions, along with a possible minor background contribution from the conductive carbon tape used to fix the samples onto the SEM stub.

The phase analysis of the TiO_2 thin film was performed using a Confotec NR500 3D Scanning Raman Spectrometer-Microscope (SOL Instruments Ltd., Minsk, Belarus). Excitation was supplied by a solid-state diode laser operating at a wavelength of $\lambda = 473$ nm. The incident beam was focused onto the sample surface using a 100× (NA = 0.95) optical objective.

3. Results and Discussion

3.1. Calculation of Ar and Xe Ion Parameters in the TiO_2/Si Structure

The electronic and nuclear energy losses of 70 MeV Ar and 220 MeV Xe ions in a multilayer target consisting of a 100 nm thick TiO_2 film on the macroPSi substrate were calculated using the SRIM-2013 software with the TRIM module. The results are presented in Table 1 and Figure 3. The ions were incident perpendicular to the target surface. When modelling the solid phase, the density of the TiO_2 layer was set to 3.89 g/cm^3, which corresponds to the anatase phase identified by Raman spectroscopy, as will be shown below. The silicon substrate was represented as a porous medium with a density of 2.329 g/cm^3. In Table 1, the calculated values of electronic (S_e) and nuclear (S_n) energy losses are given separately for each target material and ion species. Within the 100 nm thick TiO_2 layer with anatase density, values of S_e = 23.340 keV/nm and S_n = 0.072990 keV/nm were obtained for 220 MeV Xe ions, while S_e = 6.768 keV/nm and S_n = 0.008917 keV/nm were determined for 70 MeV Ar ions. Within the silicon constituent of the substrate, the values for Xe ions are S_e = 14.610 keV/nm and S_n = 0.047790 keV/nm, whereas for Ar ions they are S_e = 4.263 keV/nm and S_n = 0.005862 keV/nm (Figure 3). The projected ranges in Si are 26.02 µm for Xe and 21.01 µm for Ar.

Table 1. Parameters of 70 MeV Ar and 220 MeV Xe ions in the TiO_2/Si structure.

Material	Incident Ion Energy	S_e (keV/nm)	S_n (keV/nm)
TiO_2, anatase model	Xe, 220 MeV	23.340	0.072990
TiO_2, anatase model	Ar, 70 MeV	6.768	0.008917
Si, dense constituent	Xe, 220 MeV	14.610	0.047790
Si, dense constituent	Ar, 70 MeV	4.263	0.005862

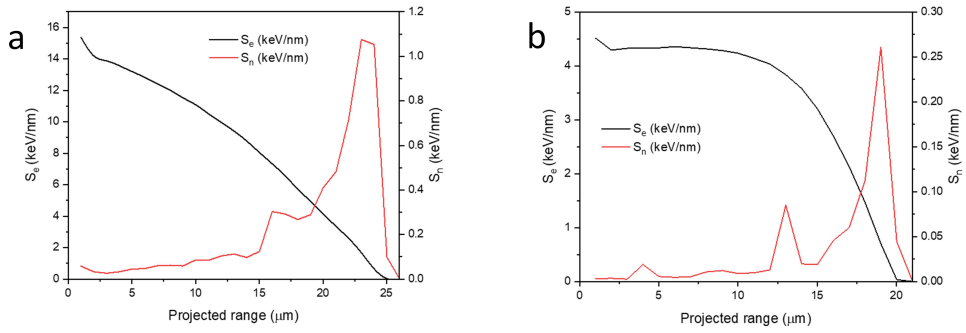


Figure 3. Electronic and nuclear energy losses of (**a**) 220 MeV Xe and (**b**) 70 MeV Ar ions within the TiO_2/Si structure.

It should be noted that due to the massive difference in scale between the ultra-thin TiO_2 capping layer (100 nm, corresponding to just 0.1 µm) and the total projected ion ranges (21–26 µm), the energy loss transformations within the oxide film are confined to a single-pixel region at the outermost surface (origin point) of the profiles in Figure 3. The precise initial stopping powers at the very entrance of each individual constituent are therefore compiled explicitly in Table 1 to ensure numerical accuracy, while Figure 3 illustrates the macroscopic energy dissipation behavior throughout the depth of the entire macroPSi framework.

Electronic energy losses predominate over nuclear losses in both materials. When evaluating the possibility of track formation, it is necessary to compare the electronic energy losses with the track formation threshold. For anatase-phase TiO_2, Rath et al. reported a threshold value of $S_{e,\mathrm{th}}$ = 7.1 ± 0.8 keV/nm [28]. The calculated S_e value for Xe ions

in TiO_2 significantly exceeds this threshold. For Ar ions, the S_e value is slightly below the central estimation of the threshold but falls within the specified uncertainty interval. Therefore, Ar ion irradiation is considered a near-threshold regime. Such a comparison with literature data is applicable within the framework of the anatase model and does not serve as a universal criterion for the formation of continuous amorphous tracks in coatings obtained by ALD.

3.2. Morphology of Ag-Free and Ag-Decorated MacroPSi/TiO_2 Substrate

The SEM images of the Ag-free samples (Figure 4a–c) show visible changes in the TiO_2 coating morphology after the ion bombardment. Prior to ion irradiation (Figure 4a), the outlines of the coating on the sample cross-sections are distinct. Measurements and averaging across 100 individual pores revealed a thickness of approximately 100 nm. Following exposure to both ion species, differentiating the boundary between the TiO_2 coating and the macroPSi substrate becomes difficult. Distinctly, Xe^{22+} bombardment resulted in surface reflow with the pore mouths appearing deformed and widened, whereas the original pore geometry remains visibly better preserved after Ar^{4+} irradiation (Figure 4b,c). However, the cross-sectional views demonstrate that the geometric parameters of the underlying silicon skeleton itself remained practically unchanged. This indicates that the morphological modifications observed via SEM are predominantly associated with the evolution of the titanium dioxide phase. The calculated electronic energy loss (S_e) of Xe ions within the TiO_2 film is 23.340 keV/nm, which significantly exceeds the track formation threshold reported in the literature for anatase. This is consistent with a potential contribution of localized electronic excitation to the film modification. For Ar ions, the S_e value in TiO_2 is 6.768 keV/nm, which is close to the anatase threshold. The less pronounced morphological changes observed under Ar irradiation are discussed considering this near-threshold regime. Since the two irradiation modes also differ in terms of fluence and initial ion energy, the structural discrepancies cannot be attributed solely to the differences in stopping power. The corresponding EDX spectra (Figure 4d,e) reveal variations in the elemental composition of the samples with irradiation in these two regimes. A more comprehensive discussion regarding the interaction mechanisms between the ions and the target constituents is developed below, following the morphological analysis of the Ag-decorated structures.

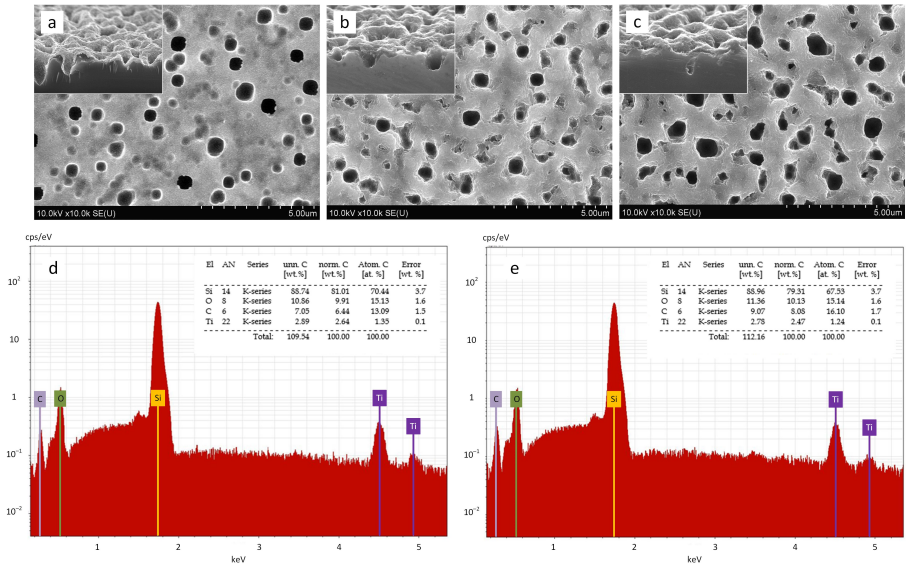


Figure 4. Morphology evolution of the Ag-free macroPSi/TiO_2 samples: SEM images of the samples (**a**) before and after (**b**) Ar^{8+}, (**c**) Xe^{22+} ion bombardment; EDX spectra of the samples after (**d**) Ar^{8+} and (**e**) Xe^{22+} ion bombardment.

SEM images of Ag-decorated macroPSi/TiO_2 show surface smoothing and changes in pore-entry geometry and nanoparticle morphology after irradiation (Figure 5a–f).

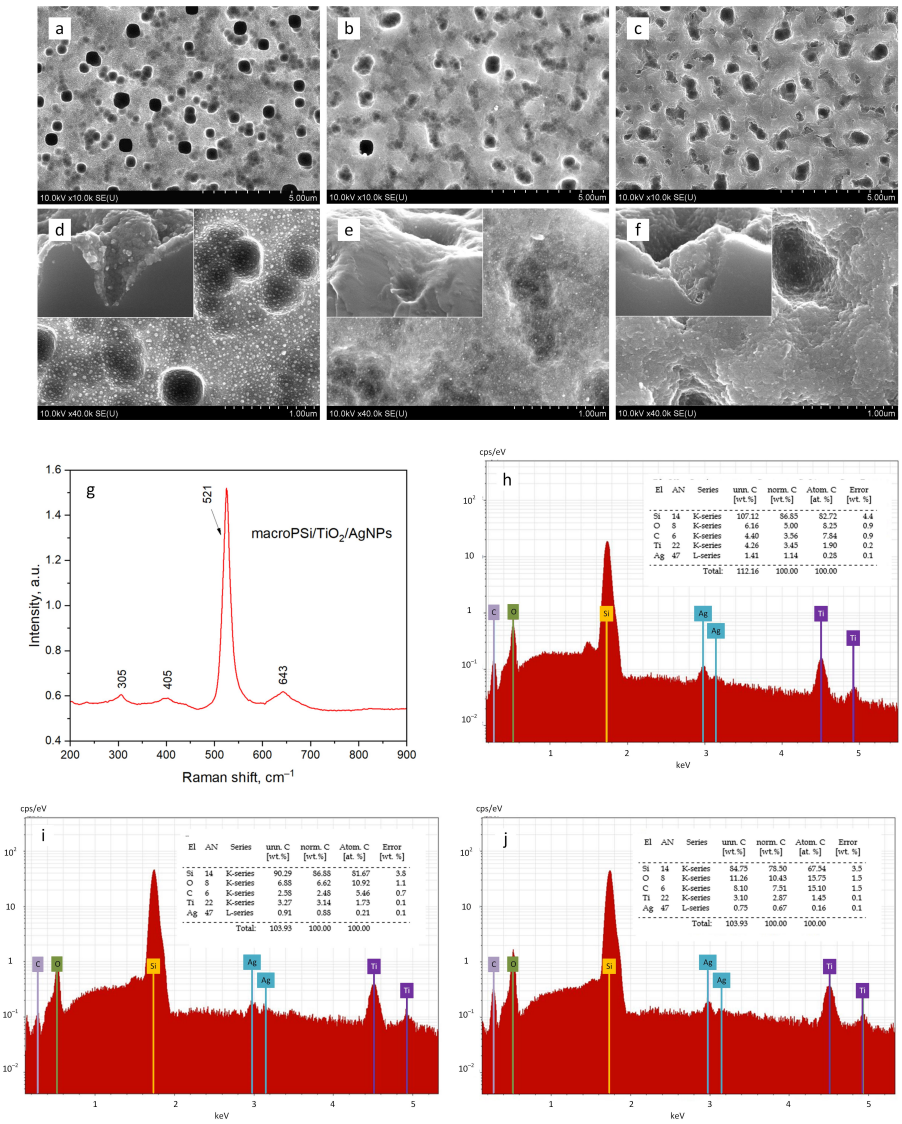


Figure 5. Morphology evolution of the Ag-decorated macroPSi/TiO_2 samples: SEM images of the samples (**a**,**d**) before and after (**b**,**e**) Ar^{8+}, (**c**,**f**) Xe^{22+} ion bombardment; (**g**) Raman spectrum of the Ag-decorated macroPSi/TiO_2 sample; EDX spectra of the samples (**h**) before and after (**i**) Ar^{8+}, (**j**) Xe^{22+} ion bombardment.

The morphology of the samples decorated with AgNPs also undergoes distinct modifications following ion bombardment. However, looking at the cross-sections, it remains difficult to discern any significant alteration in the geometry of the underlying macroPSi framework, which is evidently due to the structural robustness and massiveness of its relatively low yet wide pore walls. In contrast, both the titanium dioxide coating and the silver nanoparticles experience substantial modifications. Ar ion irradiation resulted in a blurring of the pore boundaries (Figure 5b,e), driven by localized sputtering and partial removal of the surface coating layer. Conversely, Xe ion exposure induced morphological texturing, restructuring the surface into a corrugated state (Figure 5c,f). The silver nanoparticles appear reduced in size and embedded into the modified target matrix.

Figure 5g shows the Raman spectrum of the sample prior to ion irradiation, confirming the anatase structure of the titanium oxide film. The Raman scattering profile reveals

features of both the tetragonal anatase film and the underlying Si host. The spectrum is characterized by peaks at 405 cm^{-1} and 643 cm^{-1}, which correspond to the characteristic B_{1g} and E_g active vibrational modes of the crystalline anatase TiO_2 polymorph, respectively. The predominant, narrow feature centered at 521 cm^{-1} represents a structural convolution of the first-order transverse optical (TO) phonon mode of the crystalline silicon substrate. Additionally, a weak second-order transverse acoustic phonon (2TA) scattering mode of the crystalline silicon skeleton is resolved at 305 cm^{-1}. It is important to note that a spectrum could only be recorded for the sample containing AgNPs. The Ag-free sample yielded only the spectrum of the Si substrate. This is due to the low sensitivity of spontaneous Raman spectroscopy to nanostructures such as a 100 nm-thick titanium oxide film. The AgNPs provided the SERS effect, thereby amplifying the signal from the thin titanium oxide film.

The EDX spectra (Figure 5h–j) show compositional differences between irradiation conditions but do not determine the crystalline state of the Si framework or demonstrate latent-track formation.

3.3. Evaluation of Pore Geometry and Composition

To summarize the structural changes observed in the experiments, the quantitative calculations of pore diameters and elemental composition are compiled in Figure 6. In the samples without silver, the porous matrix is highly vulnerable to the ion beams, showing a $40 \pm 0.8\%$ widening under Xe^{22+} exposure and a $14 \pm 0.3\%$ widening under Ar^{8+} exposure. When the surface is functionalized with AgNPs, this macropore expansion under high-energy Xe^{22+} is suppressed to $28 \pm 0.6\%$ and stays nearly the same ($15 \pm 0.3\%$) for Ar^{8+}. Therefore, the comparative pore-diameter histogram confirms that the presence of surface AgNPs restrains the structural dilation of the pore mouths under Xe-ion exposure.

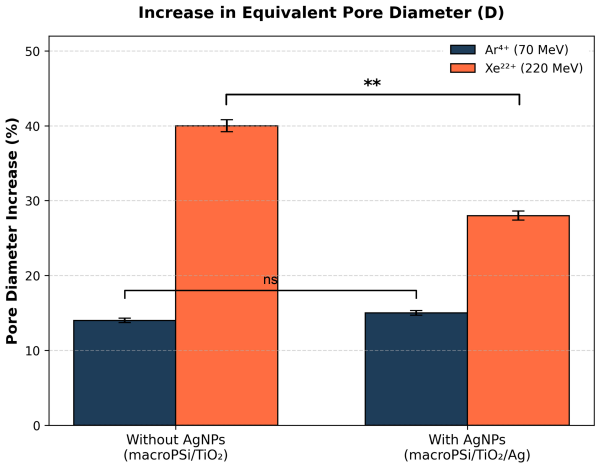


Figure 6. Histogram showing the percentage increase in the average pore diameter (D) for Ag-free and Ag-decorated macroPSi/TiO_2 samples; significance level: ns—non significant $p > 0.05$; **—$p < 0.01$.

To map out the radiation-induced elemental kinetics and evaluate the chemical shifts within the samples, the raw EDX spectroscopy datasets required methodical refinement. In the as-measured spectra, the true functional trends are heavily masked by a large background carbon signal. Since the spectrometer software operates as a closed 100% normalization loop, the severe structural damage and pore dilation driven by the heavier $^{132}Xe^{22+}$ ions lead to enhanced carbon trapping within the porous networks. In a closed calculation, this artificial carbon surge automatically compresses the relative percentages of all other constituents on the screen, creating a false instrumental illusion of a stagnant or invariant oxygen concentration between the irradiation states.

To decouple the physical transitions from these normalization artifacts, a multi-step mathematical treatment was implemented. First, to analyze the core irradiated layers, the carbon signal was completely excluded from the normalization loop, recalculating the element concentrations under a carbon-free matrix (Si + O + Ti + Ag = 100%). Second, to establish a reliable pristine control baseline for the bare TiO_2/macroPSi targets, a dedicated reconstruction was applied to the non-irradiated Ag-decorated standard. Since the localized chemical deposition of surface nanoparticles does not structurally alter the underlying framework stoichiometry, both the C and Ag peak contributions were subtracted, with the remaining matrix constituents (Si, O, and Ti) re-normalised to 100%. Furthermore, since the calculated projected ranges (21–26 μm) exceed the total thickness of the porous layer (≤1.5 μm), the incident ion beams pass completely through the capping configuration. A dominant fraction of the electron probe penetrates directly into the underlying, structurally immutable bulk crystalline silicon substrate. This bulk contribution guarantees that the total number of primary Si atoms within the analytical volume remains physically stable, serving as an ideal internal reference. When anchored against this stable silicon baseline, the objective invariant atomic ratios (X/Si) and net radiation-induced shifts were successfully extracted, as compiled in Tables 2 and 3.

Table 2. Re-normalized (carbon- and silver-free) elemental composition of the TiO_2/macroPSi matrix framework and net relative atomic variations under swift heavy ion irradiation.

Sample State	Element	As-Measured (at. %)	Carbon & Ag-Free (at. %)	Ratio to Si (**X**/Si)	Net Atomic Shift
TiO_2/macroPSi (Pristine)	Si	81.72	88.95	1.0000	0% (Reference)
	O	8.25	8.98	0.1010	0% (Reference)
	Ti	1.90	2.07	0.0233	0% (Reference)
TiO_2/macroPSi +Ar (70 MeV)	Si	70.44	81.04	1.0000	0% (Reference)
	O	15.13	17.41	0.2148	+112.7%
	Ti	1.35	1.55	0.0191	−18.0%
TiO_2/macroPSi +Xe (220 MeV)	Si	67.53	80.48	1.0000	0% (Reference)
	O	15.14	18.04	0.2242	+122.0%
	Ti	1.24	1.48	0.0184	−21.0%

Table 3. Re-normalized (carbon-free) elemental composition of Ag/TiO_2/macroPSi systems and net relative atomic variations under swift heavy ion irradiation.

Sample	Element	As-Measured (at. %)	Carbon-Free (at. %)	Ratio to Si (X/Si)	Net Atomic Shift
Ag/TiO_2/macroPSi (Pristine)	Si	81.72	88.68	1.0000	0% (Reference)
	O	8.25	8.95	0.1010	0% (Reference)
	Ti	1.90	2.06	0.0233	0% (Reference)
	Ag	0.28	0.30	0.0034	0% (Reference)
Ag/TiO_2/macroPSi +Ar (70 MeV)	Si	81.67	86.67	1.0000	0% (Reference)
	O	10.92	11.59	0.1337	+32.4%
	Ti	1.43	1.52	0.0175	−24.7%
	Ag	0.21	0.22	0.0025	−25.0%
Ag/TiO_2/macroPSi +Xe (220 MeV)	Si	67.54	79.55	1.0000	0% (Reference)
	O	15.75	18.55	0.2332	+131.0%
	Ti	1.45	1.71	0.0215	−7.7%
	Ag	0.16	0.19	0.0023	−30.9%

To isolate the exact spatial localization of the captured oxygen influx, a quantitative sub-lattice stoichiometric balance was subsequently performed on these refined coordinates. Assuming that the titanium atoms within the functional coating maintain their thermodynamically stable dioxide coordination (TiO_2) under these fluences (consistently verified by the B_{1g} and E_g active modes in the Raman scattering profiles), the atomic fraction of oxygen bound strictly to the titanium sub-lattice is defined as $2 \times \text{at.}\%_{\text{Ti}}$. The remaining net oxygen

content localized exclusively along the internal silicon pore walls (O_{Si}) can thus be isolated using the following subtraction framework:

$$\text{at.\%}_{\text{O, Si}} = \text{at.\%}_{\text{O, total}} - 2 \cdot \text{at.\%}_{\text{Ti}} \quad (1)$$

To track the true oxidation progression independent of any relative software shifts, we introduce the silicon oxidation index, defined as the O/Si atomic ratio. For the mathematically reconstructed pristine baseline, the initial oxidation index yields a value of 0.1010 for both target configurations, reflecting the background oxidation state of the un-irradiated macroPSi matrix walls. Following 70 MeV Ar^{8+} bombardment, the matrix index for the bare framework increases to 0.2148 (a 2.1-fold expansion, marking a +112.7% oxygen gain), which is substantially higher than the index observed in the Ag-decorated counterpart (0.1337, a +32.4% gain). This discrepancy highlights the effective mechanical shielding provided by the surface silver phase under the near-threshold Ar regime, where the nanoparticles intercept a fraction of the incident ion energy and suppress defect generation in the silicon walls.

Conversely, under the high-energy 220 MeV Xe^{22+} exposure, the local oxidation index of the bare matrix expands to 0.2242 (a 2.2-fold increase, or +122.0% oxygen gain), converging closely with the value recorded for the Ag-decorated system (0.2332, a +131.0% gain). This convergence indicates that under the intense electronic energy loss regime of Xe ions, the density of radiation-induced point defects and dangling bonds within the silicon skeleton reaches a state of near-saturation. Consequently, the volume of subsequent ambient oxygen trapping is primarily dictated by the high concentration of structural defects along the pore walls, rendering the presence or morphological reflow of the surface silver phase secondary in defining the ultimate oxidation limits of the macroPSi framework.

Under Xe^{22+} irradiation, the intense electronic energy leads to localized high-temperature zones in the sample. This induces two processes:

- The discrete surface AgNPs undergo not only sputtering but also melting and liquid-phase redistribution that caps and protects the pore mouths, suppressing direct surface sputtering. This explains why the presence of AgNPs successfully restrains pore widening under Xe (+28.0% vs. +40.0% for the bare matrix in Figure 6).
- Beneath these protective AgNPs, intense ion-beam mixing and interdiffusion are promoted, driving Ti atoms into the macroPSi channel walls rather than letting them escape into the vacuum. Since the redistributed Ti remains partially locked within the silicon skeleton probed by EDX spectroscopy, the registered apparent titanium loss is minimal (−7.7%).

Under Ar^{4+} irradiation, the lower energy and electronic stopping power are insufficient to drive efficient silver reflow and titanium diffusion. In the absence of both silver wetting and thermal intermixing, conventional ballistic sputtering dominates, severely eroding both the AgNPs and the underlying TiO_2 layer from the pore mouths, leading to a much higher net titanium loss (−24.7%).

4. Conclusions

Multilayer macroPSi/TiO_2 and macroPSi/TiO_2 structures decorated with AgNPs were modified by irradiation with 70 MeV Ar^{8+} and 220 MeV Xe^{22+} ions. SRIM/TRIM calculations for the multilayer target demonstrated that electronic energy losses predominate over nuclear losses in both materials. Within the TiO_2 coating with an anatase structure, the S_e values are 23.340 keV/nm for Xe^{22+} and 6.768 keV/nm for Ar^{8+}. For Xe^{22+}, this value exceeds the track formation threshold in anatase reported in the literature, whereas for Ar^{8+} it is close to this threshold. In Si, the corresponding values are 14.610 and 4.263 keV/nm.

The influence of irradiation with 70 MeV Ar^{8+} and 220 MeV Xe^{22+} ions on the pore geometry has been established. In the Ag-free samples, the average pore diameter increased by $(40 \pm 0.8)\%$ after Xe^{22+} irradiation and by $(14 \pm 0.3)\%$ after Ar^{8+} irradiation. The obtained results allow for a discussion on the energy transfer to the electronic subsystem, taking into account the properties of each material. In the samples decorated with Ag nanoparticles, surface smoothing and pore mouth widening of $(15 \pm 0.3)\%$ after Ar^{8+} irradiation and $(28 \pm 0.6)\%$ after Xe^{22+} irradiation were observed. These morphological differences provide a solid rationale for further investigations into the interfaces between the Ag nanoparticles and the coating, as well as their influence on the radiation-induced modification of the structure.

Author Contributions: Conceptualization, H.B. and A.D.; methodology, D.L.; software, Z.N.; validation, V.M., V.K. and Z.N.; formal analysis, A.B.; investigation, A.B., D.L. and Z.N.; resources, H.B. and A.D.; data curation, H.B.; writing—original draft preparation, V.M. and V.K.; writing—review and editing, H.B. and A.D.; visualization, H.B.; supervision, H.B., A.D. and A.A.; project administration, H.B., A.D. and A.A.; funding acquisition, H.B., A.D. and A.A. All authors have read and agreed to the published version of the manuscript.

Funding: The research was funded by the Science Committee of the Ministry of Science and Higher Education of the Republic of Kazakhstan (Grant No. AP23487881) and the Ministry of Education of Republic of Belarus (Project No. 2.5.5).

Data Availability Statement: The original contributions presented in this study are included in the article material. Further inquiries can be directed to the corresponding authors.

Conflicts of Interest: The authors declare no conflicts of interest.

References

1. Lu, N.; Zhang, M.; Jing, X.; Zhang, P.; Zhu, Y.; Zhang, Z. Electrospun Semiconductor-Based Nano-Heterostructures for Photocatalytic Energy Conversion and Environmental Remediation: Opportunities and Challenges. *Energy Environ. Mater.* **2023**, *6*, e12338. [CrossRef]
2. Huang, L.; Liow, J.; Lim, K.; Tan, K.W.; Liang, X.; Khiew, P.S.; Chiu, W.S.; Haw, C. Photothermal Assisted Interfacial Cleaning with Semiconductor-Based Sorbents: Recent Advances and Future Outlook for Effective Oil Spill Remediation. *Adv. Sustain. Syst.* **2024**, *8*, 2300659. [CrossRef]
3. Gao, F.; Wang, X.; Cui, W.; Liu, Y.; Yang, Y.; Sun, W.; Chen, J.; Liu, P.; Pan, H. Topologically Porous Heterostructures for Photo/Photothermal Catalysis of Clean Energy Conversion. *Small Methods* **2023**, *7*, 2201532. [CrossRef] [PubMed]
4. Thang, N.H.; Hien, N.C. Environmental and energy applications of green-synthesized semiconductor nanomaterials: From photocatalysis to smart sensors. *Ionics* **2026**, *32*, 2521–2556. [CrossRef]
5. Monaico, E.V.; Monaico, E.I.; Ursaki, V.V.; Tiginyanu, I.M. Porous Semiconductor Compounds with Engineered Morphology as a Platform for Various Applications. *Phys. Rapid Res. Lett.* **2023**, *17*, 2300039. [CrossRef]
6. Artsemyeva, K.; Dolgiy, A.; Bandarenka, H.; Panarin, A.; Khodasevich, I.; Terekhov, S.; Bondarenko, V. Fabrication of SERS-Active Substrates by Electrochemical and Electroless Deposition of Metals in Macroporous Silicon. *ECS Trans.* **2013**, *53*, 85–95. [CrossRef]
7. Girel, K.; Burko, A.; Zavatski, S.; Barysiuk, A.; Litvinova, K.; Eganova, E.; Tarasov, A.; Novikov, D.; Dubkov, S.; Bandarenka, H. Atomic layer deposition of hafnium oxide on porous silicon to form a template for athermal SERS-active substrates. *Appl. Phys. A* **2023**, *129*, 294. [CrossRef]
8. Abidi, J.; Assaedi, H.; Cherif, A.; Rahmani, M.; Rtimi, M.; Jradi, S. Optical properties enhancement of macroporous silicon through indium oxide deposition. *Opt. Mater.* **2026**, *178*, 118278. [CrossRef]
9. Sagidolda, Y.; Tuokedaerhan, K.; Azamat, R.; Darmenkulova, M.; Zhumatova, S.; Ibraimov, M.; Tezekbay, Y.; Zhazitov, M.; Abdullah, M.; Akilbekov, B.; et al. The effect of Ti, W, Ag and TiO_2 particles on the structural and optical properties of porous silicon obtained in various electrolytes. *Sci. Rep.* **2026**, *16*, 16820. [CrossRef] [PubMed]
10. Garzon-Roman, A.; Sanchez-Mora, E.; Romero-López, A.; De Anda-Reyes, M.E.; Zúñiga-Islas, C. Porous Silicon Working as Immobilizer of TiO_2 Decorated with Metal Nanoparticles Analyzing the Absorber and Photocatalytic Activity for Dexamethasone. *Silicon* **2025**, *17*, 1253–1266. [CrossRef]

11. Bandarenka, H.; Burko, A.; Girel, K.; Laputsko, D.; Orel, E.; Mizgailo, A.; Sharopov, U.; Podelinska, A.; Shapel, U.; Pankratov, V.; et al. Improvement of Heat Dissipation in Ag/Ni Substrates for Testing Cu-TiO_2/TiO_2-Modified Filters Using SERS Spectroscopy. *Crystals* **2023**, *13*, 749. [CrossRef]
12. Chiappim, W.; Fraga, M.A.; Maciel, H.S.; Pessoa, R.S. An Experimental and Theoretical Study of the Impact of the Precursor Pulse Time on the Growth Per Cycle and Crystallinity Quality of TiO_2 Thin Films Grown by ALD and PEALD Technique. *Front. Mech. Eng.* **2020**, *6*, 551085. [CrossRef]
13. Alasaarela, T.; Karvonen, L.; Jussila, H.; Säynätjoki, A.; Mehravar, S.; Norwood, R.A.; Peyghambarian, N.; Kieu, K.; Tittonen, I.; Lipsanen, H. High-quality crystallinity controlled ALD TiO_2 for waveguiding applications. *Opt. Lett.* **2013**, *38*, 3980. [CrossRef] [PubMed]
14. Halary, E.; Haro-Poniatowski, E.; Benvenuti, G.; Hoffmann, P. Crystallinity of titania thin films deposited by light induced chemical vapor deposition. *Appl. Surf. Sci.* **2000**, *168*, 61–65. [CrossRef]
15. Reddy, H.; Guler, U.; Chaudhuri, K.; Dutta, A.; Kildishev, A.V.; Shalaev, V.M.; Boltasseva, A. Temperature-Dependent Optical Properties of Single Crystalline and Polycrystalline Silver Thin Films. *ACS Photonics* **2017**, *4*, 1083–1091. [CrossRef]
16. Rizzo, A.; Tagliente, M.; Alvisi, M.; Scaglione, S. Structural and optical properties of silver thin films deposited by RF magnetron sputtering. *Thin Solid Film.* **2001**, *396*, 29–35. [CrossRef]
17. Molina-Reyes, J.; Romero-Moran, A.; Uribe-Vargas, H.; Lopez-Ruiz, B.; Sanchez-Salas, J.; Ortega, E.; Ponce, A.; Morales-Sanchez, A.; Lopez-Huerta, F.; Zuñiga-Islas, C. Study on the photocatalytic activity of titanium dioxide nanostructures: Nanoparticles, nanotubes and ultra-thin films. *Catal. Today* **2020**, *341*, 2–12. [CrossRef]
18. Semin, D.J.; Rowlen, K.L. Influence of vapor deposition parameters on SERS active Ag film morphology and optical properties. *Anal. Chem.* **1994**, *66*, 4324–4331. [CrossRef]
19. Meftah, A.; Djebara, M.; Khalfaoui, N.; Stoquert, J.; Studer, F.; Toulemonde, M. Thermal Spike Description of the Damage Creation in $Y_3Al_5O_{12}$ Induced by Swift Heavy Ions. *Mater. Sci. Forum* **1997**, *248–249*, 53–56. [CrossRef]
20. Ramos, S.; Bonardi, N.; Canut, B.; Bouffard, S.; Della-Negra, S. Damage creation in α-Al2O3 by MeV fullerene impacts. *Nucl. Instrum. Methods Phys. Res. Sect. B Beam Interact. Mater. Atoms* **1998**, *143*, 319–332. [CrossRef]
21. Kenbayev, D.; Sorokin, M.V.; El-Said, A.S.; Dauletbekova, A.; Saduova, B.; Aralbayeva, G.; Akilbekov, A.; Shablonin, E.; Bazarbek, A.D. Creation and Stability of Color Centers in BaF2 Single Crystals Irradiated with Swift 132Xe Ions. *Crystals* **2025**, *15*, 785. [CrossRef]
22. Orekhov, N.D.; Stegailov, V.V. Swift heavy ion track formation in nanoporous Si: Wave packet molecular dynamics study. *J. Phys. Conf. Ser.* **2018**, *946*, 012026. [CrossRef]
23. Awazu, K.; Fujimaki, M.; Ohki, Y.; Komatsubara, T. Photonic crystals of titanium dioxide fabricated by swift heavy ions. *Radiat. Meas.* **2005**, *40*, 722–729. [CrossRef]
24. O'Connell, J.; Skuratov, V.; Akilbekov, A.; Zhumazhanova, A.; Janse Van Vuuren, A. EM study of latent track morphology in TiO_2 single crystals. *Nucl. Instrum. Methods Phys. Res. Sect. B Beam Interact. Mater. Atoms* **2016**, *379*, 200–205. [CrossRef]
25. Karlušić, M.; Jakšić, M.; Lebius, H.; Ban-d'Etat, B.; Wilhelm, R.A.; Heller, R.; Schleberger, M. Swift heavy ion track formation in $SrTiO_3$ and TiO_2 under random, channeling and near-channeling conditions. *J. Phys. D Appl. Phys.* **2017**, *50*, 205302. [CrossRef]
26. Student. The probable error of a mean. *Biometrika* **1908**, *6* , 1–25. [CrossRef]
27. Seltman, H.J. *Experimental Design and Analysis*; Carnegie Mellon University: Pittsburgh, PA, USA, 2018; Chapter 6.
28. Rath, H.; Dash, B.; Benyagoub, A.; Mishra, N. Sensitivity of Anatase and Rutile Phases of TiO_2 to ion irradiation: Examination of the applicability of Coulomb Explosion and Thermal Spike Models. *Sci. Rep.* **2018**, *8*, 11774. [CrossRef] [PubMed]

Disclaimer/Publisher's Note: The statements, opinions and data contained in all publications are solely those of the individual author(s) and contributor(s) and not of MDPI and/or the editor(s). MDPI and/or the editor(s) disclaim responsibility for any injury to people or property resulting from any ideas, methods, instructions or products referred to in the content.